

# ESTIMATION OF WHEAT BIOMASS USING HYPERSPECTRAL DATA, WAVELET TRANSFORM, AND FRACTIONAL-ORDER DERIVATIVE

CUI, Y. Q.<sup>1\*</sup> – LI, C. C.<sup>1</sup> – LI, Y. C.<sup>2</sup>

<sup>1</sup>*School of Surveying and Land Information Engineering of Henan Polytechnic University 2001 Century Avenue, Jiaozuo 454000, Henan, P.R. China*  
(phone: +8613938141814; e-mail: cuiyingqi@hpu.edu.cn; lcc@hpu.edu.cn)

<sup>2</sup>*Zhengzhou Aerospace Hongtu Intelligent Mapping Co., LTD, Zhengzhou, Henan, China*  
(e-mail: 211904020026@home.hpu.edu.cn)

\*Corresponding author

e-mail: cuiyingqi@hpu.edu.cn; phone: +86-139-3814-1814

(Received 13<sup>th</sup> Dec 2023; accepted 25<sup>th</sup> Mar 2024)

**Abstract.** Biomass can reflect crop growth and nutritional status. Focusing on winter wheat as the study subject, this research processed canopy hyperspectral data from various growth stages using fractional-order differentiation (FOD) and continuous wavelet transform. The correlation between the data and biomass was analyzed, FOD spectra and wavelet energy coefficients with strong correlations were identified, and biomass models for estimating wheat during various growth stages were constructed through optimal subset regression (OSR) and support vector machine (SVM) approaches. Through the analysis of the modeling and verification results—in terms of the coefficient of determination ( $R^2$ ), root mean square error (RMSE), normalized RMSE, and other indicators—the optimal biomass estimation models for all growth stages and the growth stages with the highest accuracy were determined. The OSR and SVM models showed the highest modeling and validation  $R^2$  values of 0.92 and 0.88, respectively, while the average showed values of 0.84 and 0.71, respectively, indicating an excellent overall biomass estimation performance. The average modeling and validation  $R^2$  values at the flowering and filling stages were 0.89, 0.88 and 0.86, 0.84, respectively, demonstrating comparable biomass estimation accuracies between these two growth stages, which was higher than that at the jointing and booting stages. Thus, flowering and filling are the best growth stages for estimation. The FOD-based OSR model provided a higher estimation accuracy for the jointing and filling stages, while the FOD-based SVM model yielded for the booting and flowering stages.

**Keywords:** wheat, biomass estimation, machine learning, optimal subset regression, SVM

## Introduction

Biomass refers to the organic matter accumulated per unit area of crops in a certain period. It depends on photosynthesis in the crop growth process and serves as an essential basis for crop yield formation (Atzberger, 2013). Moreover, biomass is one of the essential physiological parameters in the wheat growth process. Changes in biomass can directly reflect the ability of crops to accumulate organic matter through net photosynthesis and reflect crop growth and nutritional status. Therefore, biomass estimation is significant for monitoring wheat growth and estimating yield. The

conventional biomass estimation approach is destructive manual measurement, which is cumbersome, time-consuming, and arduous and cannot be employed for a vast region (Liu et al., 2020).

In recent years, remote sensing (RS) technology has attracted increasing attention, owing to its high temporal and spatial resolution; moreover, it can be used for the quick and periodic monitoring of a specific area in an extensive range and is gradually applied to extract crop physiological and ecological parameters. This allows for the rapid estimation of crop biomass, and thus, RS technology has become the primary tool for estimating surface parameters and extracting yield phenotypic parameters (Chen et al., 2016).

Several researchers have studied crop biomass estimation based on RS technology. Zhou et al. (2018), Cui et al. (2015), and Zhang et al. (2009) employed hyperspectral and visible light spectral data to calculate vegetation index, red edge wavelength, red edge amplitude, maximum reflectance of a green peak, minimum reflectance of Red Valley, and other parameters, and analyzed the relationships of these parameters with potato biomass. Moreover, according to the correlation of rice biomass with wheat, a biomass estimation model for potato, wheat, rice, and other crops was constructed. Li et al. (2022), Zheng et al. (2017), and Ren et al. (2018) employed satellite RS data such as Sentinel-2, Sentinel-2A, and EO-1 Hyperion to establish biomass estimation models during different wheat growth periods to achieve the dynamic monitoring of biomass. They developed these models by constructing vegetation and spectral indices, combining them with the acquired biomass data, and using mathematical statistics or crop growth models. The analysis of the present research status indicates that the most available research uses the initial spectrum to establish the relevant index, analyze its correlation with crop biomass, and establish the crop biomass RS estimating model. Spectral differentiation technology partially eliminates the influence of environmental backgrounds such as atmospheric impact, vegetation shadow, and soil and describes the fundamental features of the crops.

Recently, crop growth monitoring through spectral differentiation technology has been considered in the literature, and many results have been obtained. Jing et al. (2021) studied the establishment of an RS monitoring model for wheat stripe rust using fractional-order differential spectrum (FODS) reflectance. The research results showed the highest correlation between the 1.2-order sub-differential spectrum and wheat stripe rust canopy disease intensity. The Gaussian process regression model constructed with the FODS index as an independent variable (IV) exhibited higher prediction accuracy than the reflectance spectral index. Rukya et al. (2019) found that the original spectrum and the spectrum after mathematical transformation were processed via 0 to 2 fractional-order differentiation (FOD), and the estimation accuracy could be improved using a differential spectrum (DS). Liu et al. (2020) studied the correlation between potato biomass and spectral data under various differential orders and found that the differential order of 1.6 could describe a strong correlation between potato spectral reflectance (SR) and biomass. Jiang et al. (2010) verified the correlation between spectral differential

indices with different orders and canopy chlorophyll density in the presence of stripe rust. They identified the optimal spectral differential indices with a strong correlation, established a model for estimating wheat canopy chlorophyll density, and achieved good results. Koppe et al. (2012) combined a hyperspectral index and the microwave backscattering coefficient to conduct multiple regression analysis, which resulted in improved biomass estimation precision. Yue et al. (2018) established winter wheat biomass estimation models through eight methods—artificial neural network, multiple linear regression, decision tree regression, improved binary regression tree, partial least squares, random forest, support vector machine (SVM), and principal component analysis—and explored the models' stability and anti-noise capability.

FOD can realize the refinement of spectral data, utilize the information easily overlooked via ordinary differentiation, effectively eliminate image background noise, and comprehensively exploit the potential data in the spectrum (Huang et al., 2012; Zhao et al., 2020). Scholars have extensively employed FOD in various areas. Lv et al. (2021) studied the correlation between 0- to 2-order differential SR and leaf chlorophyll content. They derived the correlation coefficient (CC) of every fractional-order differential and leaf chlorophyll content and compared and verified the curve variation rule of CC. Zhang et al. (2017) analyzed SR containing 11 fractional orders between 0 and 1 (with an increasing step of 0.1) and verified the correlation between the differential value of all orders and the acquired  $\text{Cu}^{2+}$  content in corn leaves. The results indicated that FOD could describe the correlation between the SRs of various bands and the  $\text{Cu}^{2+}$  content in leaves and expand the selection space for characteristic bands more effectively than ordinary first-order differentiation. Zhang Zhitao et al. (2020) verified the potential of estimating the content of desert soil organic matter via FOD technology integrated with an SVM classification random forest model. FOD provided higher model accuracy and robustness than integer-order differentiation. Li et al. (2021) performed hyperspectral data processing with FOD; verified the correlation between FODS and wheat chlorophyll content; and employed stepwise regression analysis, SVM, and artificial neural network to establish a chlorophyll content estimation model. Spectral signal transformation can increase its sensitivity to crop biomass. Continuous wavelet transform (CWT) can reduce noise, enable spectral data decomposition, and yield more spectral locations and representative coefficients (Ebrahimi and Rajaei, 2017). The wavelet coefficients derived via CWT can influence the inversion of heavy metals in crop canopies and phenotypic coefficients. Yu et al. (2016) explored the feasibility of CWT technology in the hyperspectral inversion of soil organic matter under various soil and land use types. CWT resulted in improved precision and robustness of the model compared with integer-order differentiation. Liu et al. (2019) used hyperspectral data, coupled with CWT and a random forest approach, to construct a model for estimating nitrogen content in summer maize and estimated nitrogen content via RS technology. Wang et al. (2020) and Tan et al. (2021) employed univariate linear regression, SVM, and partial least square approaches to establish models for estimating winter wheat leaf water content and corn canopy

chlorophyll content after the application of CWT to spectral information. These CWT-integrated methods outperformed conventional methods. Li et al. (2021) applied CWT to hyperspectral data and used a machine learning approach to establish a winter wheat biomass estimation model.

According to the preprocessing of hyperspectral data, this paper focuses on winter wheat as the study subject. FOD transform and CWT are performed, the correlation between FODS and wavelet energy coefficient (WEC) and wheat biomass is analyzed, and the wheat biomass estimation model at various growth stages (GSs) is established using optimal subset regression (OSR) analysis and SVM, and the accuracy of the model is verified. The best estimation model for all growth periods and the optimal estimation growth interval for biomass are optimized. This provides a new technical approach for the RS-based estimation of crop biomass.

## Materials and Methods

### *Study Region and Experimental Design*

The study region is Yongxingtun Village, located in Shanyang District, Jiaozuo City, Henan Province. It is located at 113.27° east longitude and 35.17° north latitude. The climate in the experimental area falls under a typical warm, mild, sub-humid monsoon climate characterized by a windy and dry spring, a rainy and hot summer, a cool autumn, and a dry and cold winter. The region is characterized by abundant sunshine, a mild climate, and abundant precipitation. The average annual sunshine duration is approximately 2300 hours, with an annual mean precipitation of 584 mm and an average frost-free period lasting for 228 days (Yan et al., 2007). In the study area, 16 experimental plots were established, each measuring 48 square meters (6 m × 8 m). These plots were replicated three times, resulting in 48 plots. The sowing density for all plots was set at 4.89 million plants per hectare, and two varieties were planted: Jing 9843 (variety 1, P1) and Zhongmai 175 (variety 2, P2). Four nitrogen fertilizer (urea) treatment levels were applied: 0 kg/ha (N1), 195 kg/ha (N2), 390 kg/ha (N3), and 585 kg/ha (N4). In terms of water treatment, three levels were implemented: rainfed (W1, no irrigation), normal water (W2, irrigation with a volume of 146 mm), and double the normal water (W3, irrigation with a volume of 292 mm). Apart from nitrogen fertilizer treatment, base fertilizers consisting of 375 kg/ha superphosphate and 150 kg/ha potassium sulfate were applied uniformly to all plots. All plots were subjected to similar field management practices. The terrain of the experimental field was flat, with a total of 48 experimental plots established. Each plot measured 6 m × 8 m, and there were three replications in total, with every 16 plots forming one repetition. *Figure 1* provides an overview of the study region and the experimental setup.

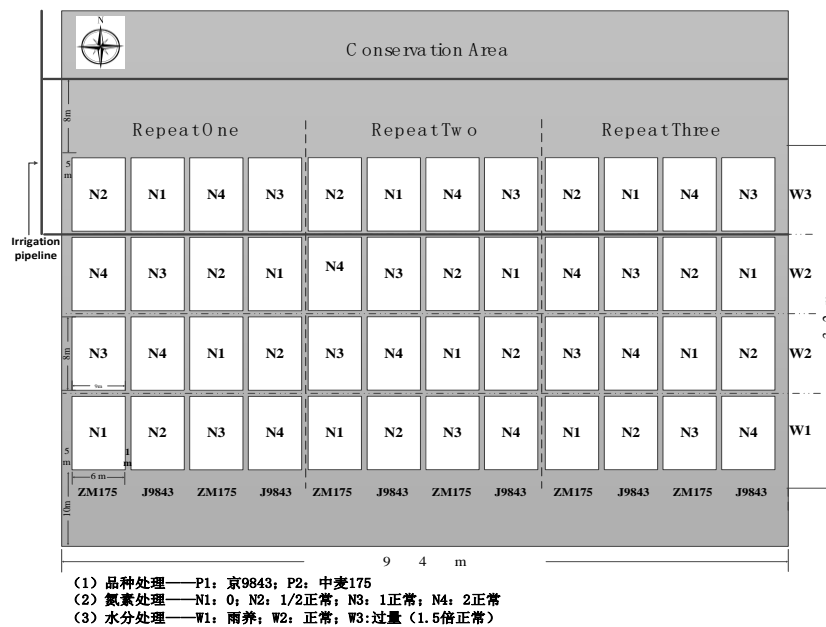
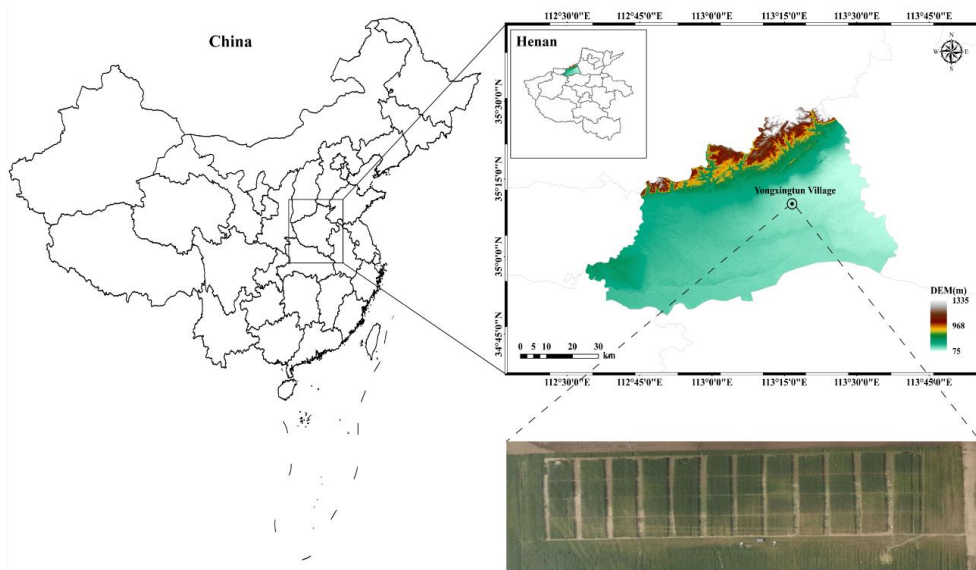


**Figure 1.** The overview of the study region and experimental design. (J9843 stands for Jing 9843, ZM175 stands for Zhongmai 175)

### Data Acquisition

Canopy hyperspectral and biomass data were acquired at the jointing, booting, flowering, and grain-filling stages of the wheat in 2018 and 2019, respectively.

### Determination of Canopy Hyperspectral Data

Hyperspectral canopy data were acquired using the Field SpecFR Pro 2500 spectrometer made by the American ASD Incorporated (Analytical spectra devices, Inc).

Figure 2 is the photo of spectrometer. The data acquisition time was from 10:00 to 14:00 Beijing time, and the weather was clear. During data collection, the sensor probe had a field of view of 25° and was positioned vertically downward, approximately 1.0 m above the winter wheat canopy. To mitigate the impact of external weather variations on spectral measurements, a whiteboard was used for spectrometer calibration both before and after all measurements (the reflectance of the whiteboard was set to 1, resulting in the obtained target spectrum being relative reflectance). Each plot was sampled 10 times, and the average value was considered as the plot canopy's SR. Owing to the varying spectral sampling intervals of the spectrometer in different bands, the spectral resampling interval was initially set to 1 nm after spectral data collection. Subsequently, the Savitzky–Golay filter in the ViewSpecPro software was applied to smoothen the spectrum, eliminating spectral noise and improving the reliability of the spectral data-to-noise ratio. Additionally, because the absorption band of water vapor significantly affected the wavelength range of 1351–2500 nm, this study focused on hyperspectral reflectance (HR) in the range of 350–1350 nm.



**Figure 2.** The Field SpecFR Pro 2500 spectrometer

### *Determination of Biomass*

The biomass of winter wheat was obtained through drying method. Random sampling method refers to randomly selecting 10 samples from areas with uniform growth of winter wheat in each community. Brought the collected samples back to the laboratory for organ (stem, leaf, ear) separation and other processing. Then put it into a paper bag. After that, the samples were placed in an oven for 20 minutes, with the temperature set to 105 °C. The treated plant samples were then baked at 80 °C for over 48h until a constant weight was achieved. The resulting dry weight (P) was divided by the corresponding sampling area (S) to calculate the biomass index (BI).

$$BI = P/S \quad (\text{Eq.1})$$

where BI stands for the biomass index, P stands for the dry weight, S describes the sampling area.

## **Data Processing Methods**

### *Fractional-Order Derivative Processing*

As a primary mathematical tool, fractional-order derivatives have been extensively used in image enhancement and signal analysis (Yang et al., 2008; Wang et al., 2011; Khahar et al., 2019; Hong et al., 2018). Conventional integer-order derivatives neglect information relevant to crop physiological and biochemical factors, which can impact the model's precision. FOD can help eliminate noise, refine local information in hyperspectral data, and extract detailed information. Popular definitions for fractional-order derivatives include Riemann-Liouville, Caputo, and Grünwald-Letnikov (Zhao et al., 2020). In this study, the Grünwald-Letnikov differential form is employed for processing hyperspectral canopy data, as defined in *Equation (1)*:

$$\frac{d^\alpha f(\lambda)}{d\lambda^\alpha} = f(\lambda) + (-\alpha)f(\lambda-1) + \frac{(-\alpha)(-\alpha+1)}{2}f(\lambda-2) + \dots + \frac{\Gamma(-\alpha+1)}{m!\Gamma(-\alpha+1)}f(\lambda-m) \quad (\text{Eq.2})$$

where  $\Gamma(\cdot)$  stands for the Gamma function,  $\lambda$  describes the corresponding wavelength,  $m$  denotes the difference between the differential's upper and lower limits, and  $\alpha$  is an arbitrary order.

### *Continuous Wavelet Transform (CWT)*

Wavelet transform (WT) is a data processing method developed from the Fourier transform. It incorporates the advantages of the Fourier transform while enabling multi-scale refinement analysis of functions or signals for information extraction. WT is often employed in processing various types of noisy signals. This approach can decompose complex signals into wavelet components with varying scales (frequencies), efficiently extracting weak information from the signal, fully describing local features, and offering time-frequency localization and multi-scale capabilities (Miao et al., 2020; Peng et al., 2021). WT is primarily categorized into CWT and discrete WT. CWT is a mathematical linear transformation method that can more easily process and interpret the contained spectral information and is widely used in hyperspectral data processing (Zhang et al., 2019). In this study, CWT is utilized to decompose the HR and various wavelet energy coefficients (WECs) at different scales. The wavelet coefficients include the decomposition scale (DS) ( $i = 1, 2, \dots, m$ ) and the band ( $j = 1, 2, \dots, n$ ). Thus, the one-dimensional HR is transformed into a two-dimensional WEC using CWT. The computation formula is as follows:

$$W_f(a,b) = \int_{-\infty}^{+\infty} f(\lambda)\Psi_{a,b}(\lambda)d\lambda \tag{Eq.3}$$

$$\Psi_{a,b}(\lambda) = \frac{1}{\sqrt{a}}\Psi\left(\frac{\lambda-b}{a}\right)$$

where  $f(\lambda)$  stands for the HR,  $\lambda$  describes the spectral band in the interval 350–1350 nm,  $\Psi_{a,b}$  describes the wavelet basis function,  $a$  represents the scaling parameter, and  $b$  describes the translation parameter.

### Modeling Method

With the improvement of big data and computer processing capabilities, machine learning has gradually become a hot topic in the field of smart agriculture research. After nearly forty years of development, numerous classic machine learning algorithms have emerged. Among them, Optimal Subset Regression (OSR) and Support Vector Machine (SVM) have been widely applied in fields such as agriculture, medicine, economics, biology, criminal psychology, and engineering technology (Wu et al., 2007; Liu et al., 2018; Yang et al., 2019) According to previous research, both of these machine learning algorithms have shown good performance in crop phenotype estimation (Wang et al., 2020; Zhang et al., 2022). This paper chooses these two machine learning algorithms to construct biomass estimation models of winter wheat. The principles and modeling methods of these two methods are as follows.

#### Optimal Subset Regression (OSR)

OSR is an approach that combines the candidate independent variables (IVs) into a model subset for regression modeling. For a model with  $n$  IVs, the optimum subset can establish  $2^n - 1$  subset models. The selection criteria for the optimum subset involve maximizing the  $R^2$  (Adjusted  $R^2$ , Adj.  $R^2$ ) and selecting the best model with the optimal combination of IVs (Zhao et al., 2020; Cai et al., 2020).

$$Adj \cdot R^2 = 1 - \frac{RSS / (n - k - 1)}{TSS / (n - 1)} \tag{Eq.4}$$

$$RSS = \sum_{i=1}^n (y_i - \hat{y}_i)^2 \tag{Eq.5}$$

$$TSS = \sum_{i=1}^n (y_i - \bar{y})^2 \tag{Eq.6}$$

where RSS denotes the residual sum of squares; TSS is the squared sum of deviations;  $y_i$  and  $\hat{y}_i$  represent the acquired and estimated values, respectively;  $\bar{y}$  describes the

estimation of the acquired one;  $n$  and  $k$  represent the number of samples and IVs, respectively; and  $i$  denotes the sample ID.

### *Support Vector Machine (SVM)*

SVM is a new learning method introduced by Vapnik et al. in 1995, which utilizes statistical learning. This algorithm is an implementation of the structural optimal risk theory. It projects the kernel function into high-dimensional space and finds the optimal hyperplane in that space. This approach can effectively address the problems of the curse of dimensionality and overfitting, demonstrating excellent generalization capabilities and robustness. SVM is commonly used for pattern identification and classification and is increasingly applied in various fields of machine learning, including few-shot regression analysis (Lin et al., 2013). When SVM is used for small sample regression analysis, it can directly derive an optimal model with limited data, mitigating issues such as “dimension disaster” and “over-learning” to some extent.

### *Correlation Analysis*

CC is employed for correlation analysis (CA). The CC is calculated according to the covariance and the standard deviation of the corresponding random variable. It ranges from  $-1$  to  $1$ , with a larger absolute value indicating a more significant correlation between the two variables. The computation equation is given by *formula (7)*:

$$\rho_{X,Y} = \frac{\text{cov}(X,Y)}{\sigma_X \sigma_Y} = \frac{E(XY) - E(X)E(Y)}{\sqrt{E(X^2) - E^2(X)} \sqrt{E(Y^2) - E^2(Y)}} \quad (\text{Eq.7})$$

where  $\rho_{X,Y}$ ,  $\text{Cov}(X,Y)$ , and  $\sigma$  describe the CC, covariance, and standard deviation of random variables, respectively.

### *Model Accuracy Evaluation*

Seventy-five percent of the sample data were selected for constructing the model, while the remaining 25% of the sample data were used to evaluate the model’s precision. The coefficient of determination ( $R^2$ ), root mean square error (RMSE), and normalized root mean square error (nRMSE) are chosen as measures for assessing the model’s precision. The calculation formula for each evaluation index is as follows:

$$R^2 = \frac{\sum_{i=1}^n y_i - \bar{y}}{\sum_{i=1}^n x_i - \bar{y}} \quad (\text{Eq.8})$$

$$RMSE = \sqrt{\frac{\sum_{i=1, j=1}^n (x_i - y_i)^2}{n}} \quad (\text{Eq.9})$$

$$nRMSE = \sqrt{\frac{\sum_{i=1, j=1}^n (x_i - y_i)^2}{n}} / \bar{y} \quad (\text{Eq.10})$$

where  $x_i$  and  $y_i$  describe the acquired and estimated values, respectively;  $\bar{y}$  describes the average value;  $i$  represents the sample ID, and  $n$  describes the number of samples.

Generally, the higher the  $R^2$ , the smaller the RMSE, which means the better the modeling effect.  $nRMSE \leq 10\%$ ,  $10\% < nRMSE \leq 20\%$ ,  $20\% < nRMSE \leq 30\%$ , and  $nRMSE > 30\%$  indicate excellent, good, moderate, and poor agreements between the acquired and estimated values, respectively.

## Results and Analysis

### *Wheat Biomass Estimation Using Fractional-Order Derivatives*

#### *Correlation Analysis of Raw Spectra and FODS with Wheat Biomass*

Grünwald–Letnikov differentiation with fractional orders ranging from 0 to 2 and a step size of 0.1 was employed to perform FOD on the primary hyperspectral data. A comparison was conducted with the original spectra, first-order differentiation, and second-order differentiation spectra. Twenty FOD transformations were applied to the canopy raw spectra at various GSs. *Figures 3 and 4* illustrate the correlations between the raw spectra and DSs of all orders and BI for different fertility intervals. Additionally, 10 DSs with high correlations were selected, and their BI correlation matrices are presented in *Figure 5*.

Analysis of *Figures 3–5* yields the following results:

As depicted in *Figure 3a*, the correlation between raw SR and BI was analyzed at the jointing stage. The original spectrum exhibited a significantly negative correlation with BI at the 0.01 level in the band interval of 350–717 nm and a considerably positive correlation with BI at the 0.01 level in the band interval of 735–1299 nm, with the maximum absolute value of the CC being  $|\rho| = 0.71$ . *Figure 4a* illustrates the correlation of the FODS with BI. The maximum absolute value of the CC  $|\rho|$  between all orders of DS and BI exceeded 0.71, with the maximum  $|\rho|$  of 0.77 observed at order 1. The number of spectral bands (SBs) passing the 0.01 highly significant level test exceeded 929, except for the integer orders (the first and second orders), and reached 958 at order 1.1. The corresponding orders and bands for the 10 DSs with high CCs were as follows: first order, 1292 nm; second order, 708 nm; first order, 956 nm; first order, 1146 nm; second order,

723 nm; 1.1 order, 720 nm; 1.9 order, 696 nm; 1.8 order, 696 nm; 1.1 order, 708 nm; and 1.7 order, 696 nm. *Figure 5a* presents their corresponding correlation matrix with BI.

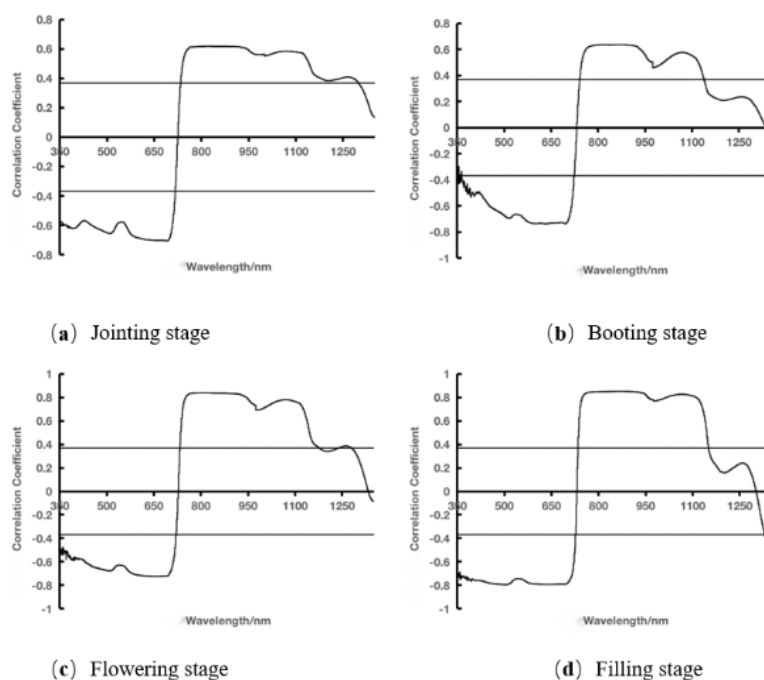


**Figure 3.** CA of original spectrum and BI at various GSs

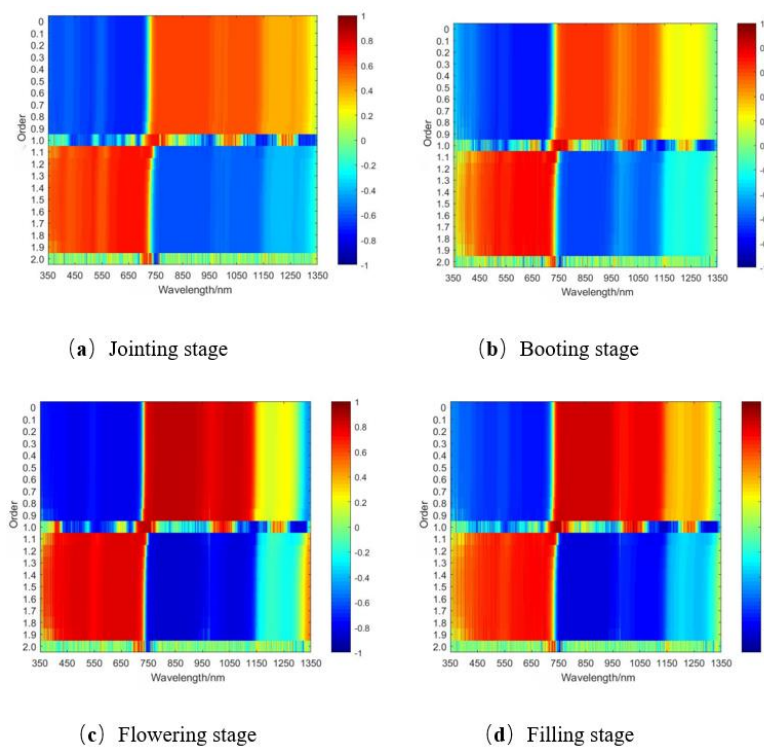


**Figure 4.** CA of FODS and BI at various GSs

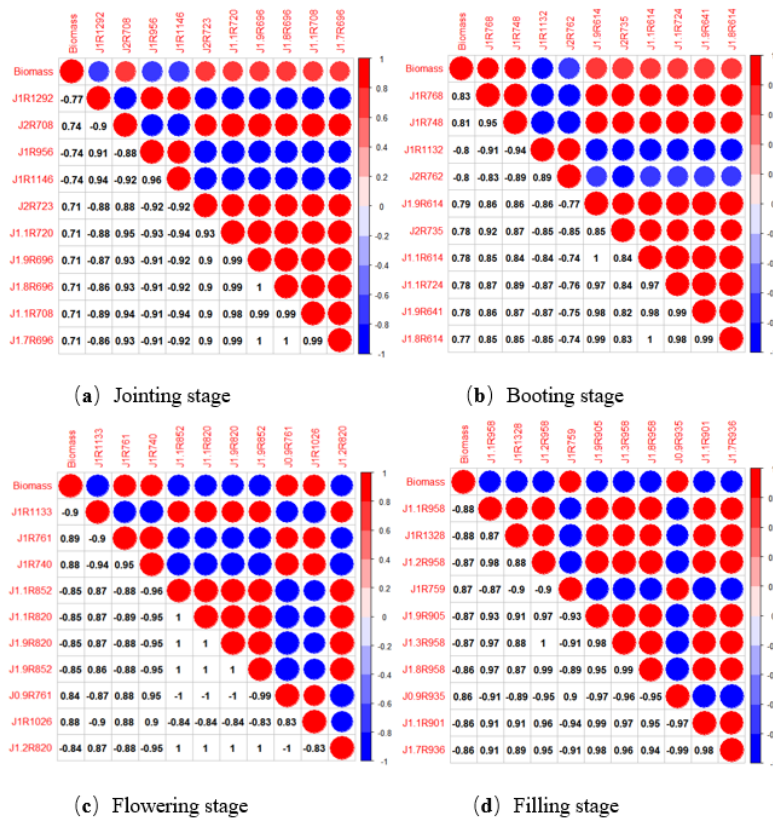


**Figure 5.** Correlation matrix diagram of selected FODS and BI at various GSs

Figure 3b illustrates the correlation between raw SR and BI at the booting stage. The original spectrum exhibited a significant negative correlation with BI at the 0.01 level in the band interval of 353–724 nm and a substantial positive correlation with BI at the 0.01 level in the band interval of 742–1138 nm, with the maximum absolute value of the CC being  $|\rho| = 0.74$ . Figure 4b shows the correlation between FODS and BI. The maximum absolute value of the CC  $|\rho|$  between all orders of DS and BI exceeded 0.74, and the maximum value of  $|\rho|$  reached 0.83 at order 1. Except for the integer orders (the first and second orders), the number of SBs passing the 0.01 highly significant level test was above 765, with a maximum of 775 bands observed for the orders of 0, 0.1, 0.2, and 0.5. The corresponding orders and bands for the 10 DSs with high CCs were as follows: first order, 768 nm; first order, 748 nm; first order, 1132 nm; second order, 762 nm; 1.9 order, 614 nm; second order, 735 nm; 1.1 order, 614 nm; 1.1 order, 724 nm; 1.9 order, 641 nm; and 1.8 order, 614 nm. Figure 5b illustrates the corresponding correlation matrices with BI.

Figure 3c presents the correlation between raw SR and BI at the flowering stage. The original spectrum displayed a significant negative correlation with BI at the 0.01 level in the band interval of 350–721 nm and a substantial positive correlation with BI at the 0.01 level in the band intervals of 734–1175 nm and 1239–1278 nm, with the maximum absolute value of the CC being  $|\rho| = 0.84$ . Figure 4c illustrates the correlation between

the FODS and BI. The maximum absolute value of the CC  $|\rho|$  between various orders of DS and BI exceeded 0.83, with the maximum  $|\rho|$  reaching 0.90 at order 1. Except for the integer orders (the first and second orders), the number of SBs passing the 0.01 highly significant level test exceeded 817, with a maximum of 855 bands observed for orders 0.3, 0.4, 0.5, and 1.3. The corresponding orders and bands for 10 DSs with high CCs were as follows: first order, 1133 nm; first order, 761 nm; first order, 740 nm; 1.1 order, 852 nm; 1.1 order, 820 nm; 1.9 order, 820 nm; 1.9 order, 852 nm; 0.9 order, 761 nm; first order, 1026 nm; and 1.2 order, 820 nm. *Figure 5c* describes the corresponding correlation matrices with BI.

*Figure 3d* describes the correlation between raw SR and BI at the filling stage. The original spectrum showed a significant negative correlation with BI at the 0.01 level in the 350–726 nm and 1330–1350 nm band intervals, and a substantial positive correlation with BI at the 0.01 level in the 735–1150 nm band interval, with the maximum absolute value of the CC being  $|\rho| = 0.85$ . *Figure 3d* illustrates the correlation between FODS and BI. The maximum absolute value of the CC  $|\rho|$  between all orders of the DS and BI exceeded 0.85.  $|\rho|$  reached 0.88 when the order was 1. The number of SBs passing the 0.01 highly significant level test exceeded 791, except for integer orders (the first and second orders), and was 815 for orders 0.3, 0.4, and 0.6. The corresponding orders and bands for 10 DSs with high CCs were as follows: 1.1 order, 958 nm; first order, 1328 nm; 1.2 order, 958 nm; first order, 759 nm; 1.9 order, 905 nm; 1.3 order, 958 nm; 1.8 order, 958 nm; 0.9 order, 935 nm; 1.1 order, 901 nm; and 1.7 order, 936 nm. *Figure 5d* depicts the corresponding correlation matrices with BI.

### *Biomass Estimation Model Construction and Analysis*

#### (1) Constructing the BI Estimating Model Using OSR

During the establishment of the BI estimation model, the OSR analysis results (*Figure 6*) indicated that eight FODSs, namely, J1R1292, J2R708, J1R956, J1.1R720, J1.9R696, J1.8R696, J1.1R708, and J1.7R696, were chosen as independent variables (IVs) to establish the OSR model at the jointing stage. *Figure 6a* presents the subset analysis results. Four FODSs, J1R768, J1R1132, J1.1R614, and J1.1R724, were chosen as IVs to establish the OSR model at the booting stage. *Figure 6b* presents the subset analysis results. Six FODSs, J1R1133, J1R761, J1R740, J1.1R820, J1.9R820, and J1.2R820, were chosen as IVs to establish the OSR model at the flowering stage. *Figure 6c* depicts the subset analysis results. Eight FODSs, J1.1R958, J1.2R958, J1R759, J1.9R905, J1.3R958, J1.8R958, J0.9R935, and J1.1R901, were chosen as IVs to establish the OSR model at the filling stage. *Figure 6d* describes the subset analysis results.

From the optimum FODS preferentially chosen at various GSs, the BI estimation models were established through the OSR approach using 75% of the sample data, while the remaining 25% of the sample data was used for model precision assessment. *Table 1* presents the  $R^2$ , RMSE, and nRMSE results in the modeling and validation of BI estimation models.

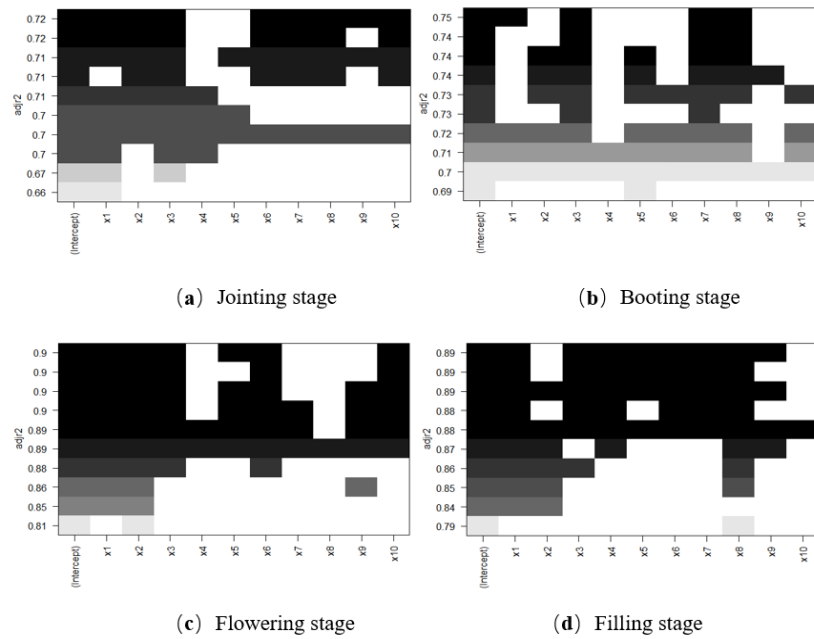


**Figure 6.** OSR analysis of the chosen FODS for the BI estimation

**Table 1.** OSR modeling results of BI estimation using FODS at various GSs

GSs	Modeling Precision			Verification Precision		
	R <sup>2</sup>	RMSE/ (kg/hm <sup>2</sup> )	nRMSE /%	R <sup>2</sup>	RMSE/ (kg/hm <sup>2</sup> )	nRMSE /%
Jointing stage	0.79	291.49	11.15%	0.51	591.92	20.48%
Booting stage	0.78	630.05	12.37%	0.67	1151.24	25.25%
Flowering stage	0.92	441.58	7.47%	0.87	624.51	10.34%
Filling stage	0.92	1989.39	58.80%	0.87	1257.70	29.32%

As presented in *Table 1*, the FODS integrated with OSR for BI estimation provided the highest estimation accuracy at the flowering stage and the lowest estimation accuracy at the filling stage, with an nRMSE of 58.80%. The estimated and acquired values showed poor agreement.

## (2) Establishing the BI Estimation Model Using SVM

The first 10 FODSs with a high correlation with BI in all growth intervals were chosen as the independent variables (IVs), while BI was the dependent variable. Seventy-five percent of the sample data were employed to establish the BI estimation models within all GSs through the SVM approach. Subsequently, 25% of the sample data was utilized for precision evaluation. *Table 2* presents the results of modeling and evaluation, including R<sup>2</sup>, RMSE, and nRMSE.

**Table 2.** BI estimating using FODS at various GSs and SVM modeling results

GSs	Modeling Precision			Verification Precision		
	R <sup>2</sup>	RMSE/ (kg/hm <sup>2</sup> )	nRMSE /%	R <sup>2</sup>	RMSE/ (kg/hm <sup>2</sup> )	nRMSE /%
Jointing stage	0.71	345.51	13.20%	0.28	700.40	24.23%
Booting stage	0.75	725.09	14.51%	0.73	1151.76	25.30%
Flowering stage	0.90	547.39	9.16%	0.88	722.13	11.89%
Filling stage	0.91	482.61	9.10%	0.83	1014.12	17.17%

As presented in *Table 2*, after the integration of FODS with SVM for BI estimation, the BI estimation accuracy at the booting stage was comparable to that at the flowering stage, which was higher than that at the filling stage.

A comprehensive analysis of BI estimation results for various GSs obtained through FODS via both OSR and SVM approaches revealed that the estimation accuracy was poor at the jointing stage. The SVM model had a modeling  $R^2$  of 0.71, and the  $R^2$  for model evaluation was only 0.28, indicating poor estimating accuracy. In contrast, the OSR model provided relatively good BI estimation accuracy with  $R^2$  values of 0.70 and 0.51 in the modeling and evaluation stages, respectively. Overall, the BI estimation performance at the booting stage surpassed that at the jointing stage, the SVM model outperformed the OSR model in terms of estimation accuracy, and the  $R^2$  values for both the modeling and evaluation of the SVM model were 0.75 and 0.73, respectively. The highest BI estimation accuracy was achieved at the flowering stage. The estimation accuracies of the OSR and SVM models were comparable, and the OSR model yielded  $R^2$  values of 0.92 and 0.87 in the modeling and validation stages, respectively, while those of the SVM model were 0.90 and 0.88, respectively. However, compared with the flowering stage, the BI estimation accuracy was lower at the filling stage. The OSR model yielded  $R^2$  values of 0.92 and 0.87, respectively, along with an nRMSE of 58.80%. The estimation effect was poor, while the SVM model demonstrated good estimation accuracy, with modeling and validation  $R^2$  values of 0.91 and 0.83, respectively.

### ***Wheat Biomass Estimation Using Wavelet Energy Coefficients***

#### ***Correlation Analysis between WECs and Biomass***

The WEC values at various scales were derived through the second-order derivative of the Gaussian function (Mexican Hat) as the CWT's wavelet basis, and by applying the CWT to the hyperspectral data of wheat canopy at all GSs, the correlation between BI and WEC at various growth intervals was investigated. *Figures 7 and 8* present the correlation graphs and matrices between WEC and BI at various fertility intervals.

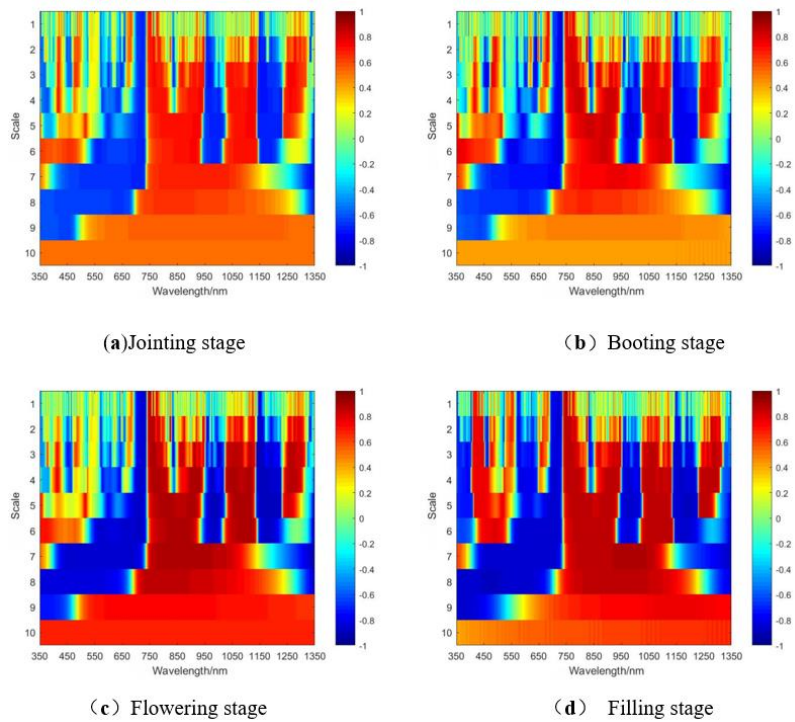


Figure 7. CA of WEC and biomass in various GSs

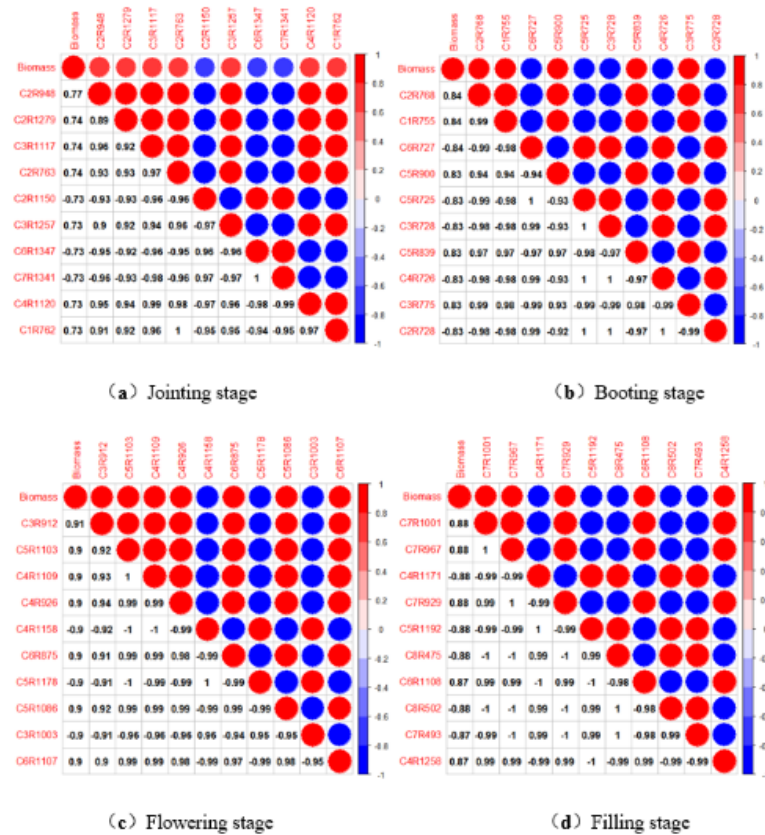


Figure 8. CA of chosen WEC and biomass in various GSs

From *Figures 7 and 8*, the following results can be drawn:

CA was conducted between the WEC and biomass at the jointing stage. As shown in *Figure 7a*, as the DS order increased, the absolute value of the CC between WEC and biomass  $|\rho|$  first increased and then decreased. When the DS order reached 10, the maximum  $|\rho|$  exceeded 0.64. When the DS order was 2, the maximum  $|\rho|$  reached 0.77. As the DS order increased, the number of SBs passing the 0.01 highly significant level test also increased. When the DS order was 10, the number of bands reached 1001. The corresponding DS orders and bands for 10 WECs with high CCs were 2, 948 nm, 2, 1279 nm, 3, 1117 nm, 2, 763 nm, 2, 1150 nm, 3, 1257 nm, 6, 1347 nm, 7, 1341 nm, 4, 1120 nm, and 1, 762 nm. *Figure 8a* presents their correlation matrix with biomass.

CA was conducted between the WEC and biomass at the booting stage. As shown in *Figure 7b*, increasing the DS order led to a decrease in the absolute value of the CC between WEC and biomass  $|\rho|$ . When the DS order was 10, the maximum  $|\rho|$  exceeded 0.64. When the DS order was 2, the maximum  $|\rho|$  was 0.84. As the DS order increased, the number of SBs passing the 0.01 highly significant level test also increased. When the DS order was 10, the number of bands was 1001. The corresponding DS orders and bands for 10 WECs with high CCs were 2, 768 nm, 1, 755 nm, 6, 727 nm, 5, 900 nm, 5, 725 nm, 3, 728 nm, 5, 839 nm, 4, 726 nm, 3, 775 nm, and 2, 728 nm. *Figure 8b* depicts their correlation matrix with LAI.

CA was performed between the WEC and biomass at the flowering stage. As shown in *Figure 7c*, as the DS order increased, the absolute value of the CC between WEC and biomass  $|\rho|$  increased first and then decreased. When the DS order was 10, the maximum  $|\rho|$  exceeded 0.74. When the DS order was 3, the maximum  $|\rho|$  reached 0.91. As the DS order increased, the number of SBs passing the 0.01 highly significant level test also increased. When the DS order was 10, the number of bands reached 1001. The corresponding DS number and bands for 10 WECs with high CCs were 3, 912 nm; 5, 1103 nm; 4, 1109 nm; 4, 926 nm; 4, 1158 nm; 6, 875 nm; 5, 1178 nm; 5, 1086 nm; 3, 1003 nm; and 6, 1107 nm. *Figure 8c* describes the corresponding correlation matrices with biomass.

The correlation between the WEC and biomass at the filling stage was analyzed. As shown in *Figure 7d*, the absolute value of the CC between WEC and biomass  $|\rho|$  decreased gradually. When the DS order was 10, the maximum  $|\rho|$  exceeded 0.86. When the DS order was 7, the maximum  $|\rho|$  reached 0.88. As the DS order increased, the number of SBs passing the 0.01 highly significant level test also increased. When the DS order was 10, the number of bands reached 1001. The corresponding DS orders and bands for 10 WECs with high CCs were 7, 1001 nm; 7, 967 nm; 4, 1171 nm; 7, 929 nm; 5, 1192 nm; 8, 475 nm; 6, 1108 nm; 8, 502 nm; 7, 493 nm; and 4, 1258 nm. *Figure 8d* presents the corresponding correlation matrices with biomass.

### Establishment and Analysis of Wheat Biomass Estimation Model

#### (1) Establishment and analysis of a biomass estimation model using OSR

The OSR analysis results (*Figure 9*) in establishing the biomass estimation model indicated that four WECs, C3R1117, C3R1257, C6R1347, and C4R1120, were chosen as IVs at the jointing stage to establish the OSR model. *Figure 9a* presents the OSR analysis results. Three WECs, C5R900, C5R725, and C3R728, were chosen as IVs to establish the OSR model at the booting stage. *Figure 9b* depicts the OSR analysis results. Five WECs, C3R912, C4R1158, C5R1178, C3R1003, and C6R1107, were chosen as IVs to establish the OSR model at the flowering stage. *Figure 9c* presents the subset analysis results. Three WECs, C4R1171, C5R1192, and C4R1258, were chosen as IVs to establish the OSR model at the filling step. *Figure 9d* depicts the subset analysis results.

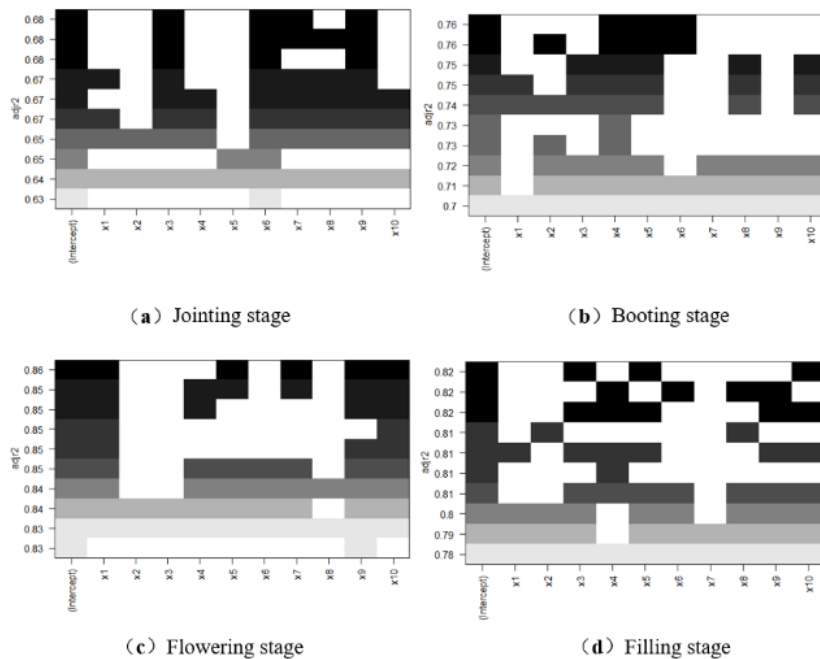


**Figure 9.** OSR analysis of WEC for estimating biomass in different GSs

From the optimum WECs chosen in various GSs, the biomass estimation models at all GSs were constructed using 75% of the sample data through the OSR approach, and 25% of the sample data were adopted to evaluate the model precision. *Table 3* presents the  $R^2$ , RMSE, and nRMSE values of the biomass estimation models.

As presented in *Table 3*, after integrating WECs with OSR for biomass estimation, the maximum precision was obtained at the flowering stage, and the modeling and verification accuracy metrics were ( $R^2 = 0.88$ , RMSE = 537.47 kg/hm<sup>2</sup>, nRMSE = 9.10%) and ( $R^2 = 0.83$ , RMSE = 740.78 kg/hm<sup>2</sup>, nRMSE = 12.42%), respectively.

**Table 3.** OSR modeling results of biomass using WEC in various GSs

Growth interval	Modeling accuracy			Evaluation precision		
	R <sup>2</sup>	RMSE/ (kg/hm <sup>2</sup> )	nRMSE /%	R <sup>2</sup>	RMSE /(kg/hm <sup>2</sup> )	nRMSE /%
Jointing stage	0.72	338.98	12.97%	0.40	670.49	22.61%
Booting stage	0.78	621.45	12.21%	0.65	1252.30	28.28%
Flowering stage	0.88	537.47	9.10%	0.83	740.78	12.42%
Filling stage	0.84	643.85	12.13%	0.81	1254.02	20.52%

## (2) Establishing the biomass estimation model via SVM

The first 10 FODSs with a high correlation with LAI in all growth intervals were chosen as the IVs, and biomass was chosen as the dependent variable. Seventy-five percent of the sample data were adopted to establish biomass estimating models within all GSs via SVM. Twenty-five percent of the sample data were then used for accuracy evaluation. *Table 4* presents the R<sup>2</sup>, RMSE, and nRMSE modeling and verification values.

**Table 4.** Biomass estimation using WEC in various GSs and SVM modeling results

Growth interval	Modeling precision			Verification precision		
	R <sup>2</sup>	RMSE/ (kg/hm <sup>2</sup> )	nRMSE /%	R <sup>2</sup>	RMSE/ (kg/hm <sup>2</sup> )	nRMSE /%
Jointing stage	0.68	368.01	14.07%	0.33	680.57	23.56%
Booting stage	0.67	778.09	15.61%	0.75	1086.29	23.78%
Flowering stage	0.87	573.18	9.66%	0.87	705.14	11.76%
Filling stage	0.85	627.94	11.82%	0.85	1070.29	17.83%

As presented in *Table 4*, biomass estimation using a combination of WECs and SVM resulted in comparable accuracy values at the flowering and filling stages, and the estimation accuracy at these stages was higher than those at the jointing and booting stages. Moreover, their corresponding modeling and validation R<sup>2</sup> values were above 0.84, and the modeling nRMSE was below 18%.

The analysis of LAI estimating results for various GSs, derived through WECs via OSR and SVM approaches, indicated that the biomass estimation accuracy at the jointing step was lower than those at the other GSs. Besides, the OSR and SVM models featured comparable estimation accuracy; the modeling and evaluation R<sup>2</sup> values of the OSR model were 0.72 and 0.40, respectively, while those of the SVM model were 0.68 and 0.33, respectively. The biomass estimation accuracy at the booting step was higher than

that at the jointing step. The OSR model provided a higher estimation accuracy than the SVM model, with the modeling and evaluation  $R^2$  values being 0.81 and 0.75, respectively. The highest biomass estimation accuracy was obtained at the flowering step. The OSR and SVM models exhibited comparable estimation accuracy, with the modeling and evaluation  $R^2$  values being 0.88 and 0.83 for the OSR model, respectively, and 0.87 and 0.87 for the SVM model, respectively. The biomass estimation impact at the filling stage was superior to that at the jointing and booting stages, and the SVM method provided a higher estimation accuracy than the OSR model, with the modeling and evaluation  $R^2$  values being 0.85 and 0.75, respectively.

## Discussion

(1) Through OSR and SVM approaches, the results of biomass estimation based on FODS and WECs for four GSs were comprehensively analyzed. The maximum modeling and validation  $R^2$  values obtained for the OSR and SVM estimation models were 0.92 and 0.88, respectively. The mean values of  $R^2$  were 0.81 and 0.70, respectively. Compared with reference (Guo et al., 2023), the modeling  $R^2$  has increased by 11%, while the validation  $R^2$  is equivalent. And compared with reference (Zhu et al., 2023), the modeling  $R^2$  is equivalent, while the validation  $R^2$  has increased by 15%. It indicates that the biomass estimation was accurate. This accuracy is related to the use of hyperspectral data, which provide high spectral resolution and valuable spectral information about ground objects. It can verify the spectral features of ground objects from various angles and orientations and provide a comprehensive description of the crops' detailed information, making it suitable for RS estimation of crop phenotypic factors. The challenge in using hyperspectral data to estimate crop biomass lies in accurately extracting the spectral information sensitive to biomass in the hyperspectral data. However, in the data collection process, environmental and background factors can introduce noise into the primary spectral data, affecting the extraction of sensitive information. FOD and WT can successfully remove the impact of noise, refine spectral data, and effectively improve the accuracy of crop biomass estimation.

(2) A comprehensive analysis of the biomass estimation effect at various GSs indicated that in the jointing stage, the maximum values of modeling and validation  $R^2$  were only 0.79 and 0.51, respectively. The estimation accuracy was lower than that at the flowering and filling stages. Only a slight difference existed between the modeling and evaluation  $R^2$  values of the quantitative estimation model; the mean modeling  $R^2$  values at the flowering stage were 0.89 and 0.88, respectively, while those at the filling stage were 0.86 and 0.84, respectively. The modeled nRMSEs were quite different, with mean values of 8.85% and 22.96%, both less than 23%. However, at the grain-filling stage, the verification nRMSE had a maximum value of 58.80% and an average value of 21.21%. In contrast, at the flowering stage, the maximum verification value of nRMSE was only 12.42%, and the mean value was 11.60%, indicating that the biomass estimation accuracy

in the flowering stage was higher than that in the grain-filling stage. Moreover, layer spectra were relatively sensitive.

(3) The biomass estimation accuracies of various approaches at different GSs were comprehensively analyzed. In the jointing stage, the OSR model using fractional-order derivative yielded better estimation results, with  $R^2$  values of 0.79 for modeling and 0.51 for evaluation. The fractional-order spectrum-based SVM model achieved the highest biomass estimating accuracy, with modeling and evaluation  $R^2$  values of 0.75 and 0.73, respectively. In the flowering stage, the fractional-order derivative-based SVM model exhibited the highest biomass estimation accuracy, with  $R^2$  values of 0.90 for modeling and 0.88 for evaluation. In the grain-filling stage, the fractional-order derivative-based OSR model yielded the highest biomass estimation accuracy, achieving modeling and evaluation  $R^2$  values of 0.92 and 0.87, respectively. This approach proves to be the optimal choice for wheat biomass estimation in various GSs.

(4) The biomass estimation effects of the OSR and SVM models using FODS and WEC were analyzed for the four growth intervals. The SVM model exhibited the highest biomass estimation accuracy, with maximum values of  $R^2$  for modeling and validation reaching 0.92 and 0.88, respectively. The mean values reached 0.84 and 0.71, respectively, because as an emerging spectral processing method, fractional-order differential transformation can allow for the effective denoising and decomposition of spectral data, extraction of hidden spectral information, and derivation of more sensitive data. This can significantly enhance the model's precision and generalization capability.

## Conclusion

In this study, hyperspectral data obtained from wheat canopies at various GSs were analyzed via FOD and CWT. CA results showed significant correlations between FODS and WEC. FODS and WEC were used in combination with OSR and SVM methods, respectively, to construct models for estimating wheat biomass in several GSs. Additionally, through the analysis of the modeling and verification of  $R^2$ , RMSE, and nRMSE indicators, the optimal biomass estimation method for all GSs and the GS with the best biomass estimation effect were selected to provide a reference for the selection of crop biomass estimation schemes. Further studies are required in the following areas:

The current study utilized the statistical regression method to estimate wheat biomass, empirically simplifying the radiative transfer process of RS. The study focused on analyzing RS and acquired data and did not consider the radiative transfer process. This omission affects the model's universality. The radiative transfer process of RS should be parameterized to alleviate the impact of uncertain errors on the estimation results.

Machine learning-based modeling is suitable for large datasets. The experimental data used in this paper were small, and overfitting phenomena can influence the model's robustness. Future research should increase the sample size to include different crop varieties and multiple years of data to evaluate the model and enhance its universality and

robustness. Limited by the experimental conditions, only sample data from one experimental area were employed, and the regional influence on the experimental data was not considered. Experimental data from different regions and observation data from multiple years should be used to train the model, to enhance its estimation capabilities.

## REFERENCES

- [1] Atzberger, C. (2013): Advances in Remote Sensing of Agriculture: Context Description, Existing Operational Monitoring Systems and Major Information Needs. – *Remote Sensing* 5(2): 949-98.
- [2] Cai, W., Zhao, S., Wang, Y., Peng, F., Heo, J., Duan, Z. (2020): Estimation of winter wheat crop stubble coverage based on Sentinel-2 spectral and texture information. – *Journal of Remote Sensing* 24(09): 1108-1119.
- [3] Chen, Z., Ren, J., Tang, H., Shi, Y., Leng, P., Liu, J., Wang, L., Wu, W., Yao, Y. Hastuya. (2016): Progress and Prospects of Agricultural Remote Sensing Research and Application. – *Acta Remote Sensing* 20(05): 748-767.
- [4] Cui, R., Liu, Y., Fu, J. (2015): Study on biomass estimation of winter wheat based on visible light spectrum and BP artificial neural network. – *Spectroscopy and Spectral Analysis* 35(09): 2596-2601.
- [5] Ebrahimi, H., Rajaei, T. (2017): Simulation of groundwater level variations using wavelet combined with neural network, linear regression and support vector machine. – *Global & Planetary Change* 148: 181-191.
- [6] Guo, Y., Jing, Y., He, J., Zhang, H., Jia, D., Wang, L. (2023): Winter Wheat Aboveground Biomass and Yield Estimation Based on Multi-Source Information from UAV Imagery. – *Journal of Henan Agricultural Sciences* 52(12): 149-161.
- [7] Hong, Y. S., Chen, Y. Y., Yu, L., Liu, Y., Liu, Y., Zhang, Y., Liu, Y., Cheng, H. (2018): Combining fractional order derivative and spectral variable selection for organic matter estimation of homogeneous soil samples by VIS–NIR spectroscopy. – *Remote Sensing* 10(3): 479.
- [8] Huang, G., Xu, L., Pu, Y. (2012): Review of Fractional Calculus in Image Processing. – *Research on Computer Applications* 29(02): 414-420+426.
- [9] Jiang, J., Chen, Y., Huang, W. (2010): Estimation of chlorophyll density in wheat canopy under stripe rust stress by hyperspectral differential index. – *Spectroscopy and Spectral Analysis* 30(08): 2243-2247.
- [10] Jing, X., Zhang, T., Zou, Q., Yan, J., Dong, Y. (2021): Construction of a remote sensing monitoring model for wheat stripe rust based on fractional differential spectral index. – *Chinese Journal of Agricultural Engineering* 37(17): 142-151.
- [11] Khahar, Y., Yang, S., Tashvlati, N. et al. (2019): Hyperspectral Estimation of soil conductivity based on fractional differential optimization spectral index. – *Journal of Ecology* 39(19): 7237-7248.
- [12] Koppe, W., Gny, M. L., Hennig, S. D., Miao, Y., Chen, L., Bareth, J. G. (2012): Multi-Temporal Hyperspectral and Radar Remote Sensing for Estimating Winter Wheat Biomass in the North China Plain. – *Photogrammetrie - Fernerkundung - Geoinformation* 3: 281-298.
- [13] Li, C., Shi, J., Ma, C., Cui, Y., Wang, Y., Li, Y. (2021): Estimation of chlorophyll content in winter wheat based on wavelet transform and fractional differentiation. – *Journal of Agricultural Machinery* 52(08): 172-182.

- [14] Li, C., Li, Y., Wang, Y., Ma, C., Chen, W., Ding, F. (2021): Estimation of Winter Wheat Biomass Based on Wavelet Energy Coefficient and Leaf Area Index. – *Journal of Agricultural Machinery* 52(12): 191-200.
- [15] Li, S., Xu, D., Fan, K., Chen, J., Tong, X., Xin, X., Wang, X. (2022): Research on aboveground biomass inversion of grassland based on UAV and satellite remote sensing. – *Remote Sensing Technology and Application* 37(01): 272-278.
- [16] Lin, H., Liang, L., Zhang, L., Du, P. (2013): Hyperspectral remote sensing inversion of wheat leaf area index based on support vector machine regression algorithm. – *Chinese Journal of Agricultural Engineering* 29(11): 139-146.
- [17] Liu, F., Wang, S., Zhang, Y. (2018): Overview on Models and Applications of Support Vector Machine. – *Computer Systems and Applications* 27(4): 1-9.
- [18] Liu, D., Nie, R., Xu, X. (2019): A nitrogen estimation model for summer maize based on continuous wavelet transform and RF algorithm. – *Barley and Cereal Science* 36(02): 42-46.
- [19] Liu, M., Li, C., Li, Z., Feng, H., Yang, G., Tao, H. (2020): Aboveground biomass estimation of winter wheat based on hyperspectral remote sensing and SAFY model. – *Journal of Agricultural Machinery* 51(02): 192-202+220.
- [20] Liu, Y., Feng, H., Sun, G., Yang, F., Yang, G. (2020): Estimation of aboveground biomass of potato based on UAV hyperspectral fractional derivative. – *Journal of Agricultural Machinery* 51(12): 202-211.
- [21] Lv, X., Xue, L., Jing, X., Zhang, C., Xu, H., Zhu, Q. (2021): Estimation of SPAD value of tobacco leaves based on hyperspectral fractional differentiation. – *Chinese Agricultural Science Bulletin* 37(24): 54-59.
- [22] Miao, M., Wang, B., Li, C., Long, H., Yang, G., Feng, H., Zhai, L., Liu, M., Wu, Z. (2020): Remote sensing estimation of the maximum net photosynthetic rate of winter wheat leaves based on continuous wavelet transform. – *Jiangsu Agricultural Journal* 36(03): 544-552.
- [23] Peng, Y., Chen, S., Chen, J., Zhao, J., Wang, C., Guan, Y. (2021): Estimation model of chlorophyll a concentration based on continuous wavelet coefficients. – *Advances in Lasers and Optoelectronics* 58(08): 431-439.
- [24] Ren, J., Wu, S., Liu, B., Chen, Z., Liu, X., Li, H. (2018): Inversion of aboveground dry biomass of winter wheat based on Hyperion hyperspectral images. – *Journal of Agricultural Machinery* 49(04): 199-211.
- [25] Rukya, S., Abduani, A., Nijati, K., Li, H., Wumuti, A., Kahar, Y., Li, X. (2019): Based on fractional differentiation Hyperspectral estimation of chlorophyll content in spring wheat. – *Journal of Wheat Crops* 39(06): 738-746.
- [26] Tan, X., Wang, Z., Zhang, J., Wang, B., Yang, F., Yang, W. (2021): Estimation of chlorophyll density in maize canopy under drought stress based on continuous wavelet transform. – *Agricultural Research in Arid Areas* 39(04): 155-161.
- [27] Wang, C., Lan, L., Zhou, S. (2011): Application of Adaptive Fractional Differentiation in Image Texture Enhancement. – *Journal of Chongqing University* 34(02): 32-37.
- [28] Wang, Y., Zhang, X., Jin, Y., Gu, X., Feng, H., Wang, C. (2020): Research on quantitative inversion of winter wheat leaf water content based on continuous wavelet transform. – *Journal of Wheat Crops* 40(04): 503-509.
- [29] Wang, X., Li, Y., Wang, R., Shi, F., Xu, S. (2020): Remote sensing inversion of surface soil organic matter at jointing stage of winter wheat based on unmanned aerial vehicle multispectral. – *Chinese Journal of Applied Ecology* 31(07): 2399-2406.
- [30] Wu, Q., Yuan, Z., Wang, X. (2007): Overview of Partial Least Squares Regression Analysis. – *Journal of Shenyang University* 19(2): 33-35.
- [31] Yan, X., Li, W., Zhao, H., Yang, L. (2007): Survey of Agroclimatic Resources and Change Characters in Jiaozuo. – *Meteorological and Environmental Sciences* 30(2): 68-71.

- [32] Yang, Z., Zhou, J., Yan, X., Huang, M. (2008): Image Enhancement Based on Fractional Differential. – *Journal of Computer Aided Design and Graphics* 3: 343-348.
- [33] Yang, J., Qiao, P., Li, Y. et al. (2019): A Review of Machine-learning Classification and Algorithms. – *Statistics and Decision* 6: 36-40.
- [34] Yu, L., Hong, Y., Zhou, Y., Zhu, Q. (2016): Construction of soil organic matter content inversion model based on continuous wavelet transform hyperspectral data. – *Spectroscopy and Spectral Analysis* 36(05): 1428-1433.
- [35] Yue, J., Feng, H., Yang, G., Li, Z. (2018): A Comparison of Regression Techniques for Estimation of Above-Ground Winter Wheat Biomass Using Near-Surface Spectroscopy. – *Remote Sensing* 10(1).
- [36] Zhang, K., Wang, R., Wang, X., Zhao, H., Han, H. (2009): A hyperspectral remote sensing estimation model for aboveground fresh biomass of spring wheat on the Loess Plateau. – *Journal of Ecology* 28(06): 1155-1161.
- [37] Zhang, W., Yang, K., Xia, X., Liu, C., Sun, T. (2017): Correlation analysis between spectral fractional differential and heavy metal copper content in maize leaves. – *Science Technology and Engineering* 17(25): 33-38.
- [38] Zhang, T., Yu, L., Yi, J., Nie, Y., Zhou, Y. (2019): Estimation of soil organic matter content by hyperspectral wavelet energy features. – *Spectroscopy and Spectral Analysis* 39(10): 3217-3222.
- [39] Zhang, Z., Lao, C., Wang, H., Karnieli, A., Chen, J., Li, Y. (2020): Hyperspectral prediction of soil organic matter content based on FOD and SVM-DFA-RF. – *Journal of Agricultural Machinery* 51(01): 156-167.
- [40] Zhang, Y., Luo, S., Wang, C., Xi, X., Nie, S., Li, D., Li, G. (2022): Combining UAV LiDAR and Hyperspectral Data for Retrieving Maize Leaf Area Index. – *Remote Sensing Technology and Application* 37(05): 1097-1108.
- [41] Zhao, Q., Ge, X., Ding, J., Wang, J., Zhang, Z., Tian, M. (2020): Spectral estimation of soil organic carbon content by combining fractional differential technology and machine learning algorithm. – *Advances in Lasers and Optoelectronics* 57(15): 253-261.
- [42] Zheng, Y., Wu, B., Zhang, M. (2017): Estimation and evaluation of aboveground dry biomass of winter wheat based on Sentinel-2 data. – *Acta Remote Sensing* 21(02): 318-328.
- [43] Zhou, Z., Jabloun, M., Plauborg, F., Andersen, M. N. (2018): Using ground-based spectral reflectance sensors and photography to estimate shoot N concentration and dry matter of potato. – *Computers and Electronics in Agriculture* 144.
- [44] Zhu, Y., Tao, X., Chen, X., Su, X., Liu, J., Li, X. (2023): Estimation of above-ground biomass of winter wheat based on vegetation indexes and texture features of multispectral images captured by unmanned aerial vehicle. – *Acta Agriculturae Zhejiangensis* 35(12): 2966-2976.